nature communications

Article

https://doi.org/10.1038/s41467-025-62432-3

Isotope-driven hydrogel smart windows for self-adaptive thermoregulation

Received: 11 November 2024

Accepted: 17 July 2025

Published online: 29 July 2025

Check for updates

Hongyi Tu[1], Tong Wang[2] ✉, Min Chen[1] & Limin Wu[1] ✉

As a cutting-edge and environmentally friendly approach, thermochromic hydrogel smart windows show great potential in combating climate change and achieving carbon neutrality. However, the substantial absorption of near-infrared (NIR) energy by H_2O poses an enormous challenge in enhancing the spectral responsiveness. Herein, we propose an ingenious concept of isotope-driven D_2O-hydrogel smart windows, which can effectively resolve the inherent issue of NIR energy absorption associated with H_2O, without compromising versatility. It facilitates near-optimal transmittance modulation across the entire solar spectrum ($\Delta\Gamma_{Sol}$ = 91.97%), demonstrating a marked enhancement in NIR modulation of transmittance ($\Delta\Gamma_{NIR}$) and reflectance (ΔR_{NIR}) by ~16% and ~31%, respectively, in comparison to conventional H_2O-hydrogel. Moreover, the integration of Ag-nanowires into D_2O-hydrogel further substantially augments the regulation of longwave infrared emissivity ($\Delta\varepsilon_{LWIR}$ = 31.89%) while preserving a comprehensive modulation ratio ($\Delta\Gamma_{Sol}$ = 66.02%, ΔR_{Sol} = 48.41%) that is not achieved by the existing thermochromic devices. This isotope-driven D_2O-hydrogel smart window provides another design strategy for future energy-efficient windows.

Buildings account for a significant proportion of global energy consumption, approximately 40%, and 33% of greenhouse gas emissions[1–6]. Windows are particularly noteworthy as the least energy-efficient components and contribute to approximately 60% of total energy loss[1,7], primarily due to their inadequate efficiency[1–3,5,7,8] and exceptionally high window-to-wall ratio in modern architectural designs[2,9]. Mitigating the thermal burden of buildings is important for efforts to combat climate change and achieve carbon neutrality[10–12]. Thermochromic smart windows have emerged as a contemporary and sustainable solution for passive energy management owing to their zero-energy consumption, straightforward design, and notable ability to dynamically modulate light in real time[1–7]. It is imperative to optimize the modulation of solar transmission and reflection ($\Delta\Gamma_{Sol}$ and ΔR_{Sol}, within the wavelength range of 0.3–2.5 μm) as well as mid-infrared emission ($\Delta\varepsilon_{LWIR}$, within the wavelength range of 3–15 μm) to dynamically control the indoor light intensity and thermal radiation during the heating and cooling cycles, thereby enhancing the energy conservation performance and environmentally adaptive capacity of smart windows.

In recent years, hydrogels have demonstrated the high-performance solar modulation capability among thermochromic smart windows due to the interaction between the polymer network and the solvent phase under external stimuli[3,7]. Near infrared (NIR, 780–2500 nm) radiation accounts for approximately 43% of total solar radiation; thus, altering the NIR state from opaque in the summer to transparent in the winter is highly desirable. Nevertheless, the substantial absorption of NIR energy by H_2O, which is typically a primary component[13], poses an enormous challenge for further performance development. Considering the transitions in vibrational energy levels resulting from infrared absorption by molecules, the atomic vibrations of H_2O and its isotope counterpart D_2O have long served as approximated harmonic oscillations[14–16] to facilitate the determination of the fundamental vibrational frequencies of diatomic molecules in the infrared spectrum. According to the diatomic molecular vibration

[1]Department of Materials Science, State Key Laboratory of Coatings for Advanced Equipment, Fudan University, Shanghai, China. [2]School of Artificial Intelligence Science and Technology, University of Shanghai for Science and Technology, Shanghai, China. ✉e-mail: wangtong@usst.edu.cn; lmw@fudan.edu.cn

equation derived from quantum mechanics, we can ascertain the fundamental frequency absorption wavenumber of the harmonic oscillator, denoted ν (cm^{-1})

$$\nu = \frac{1}{2\pi c}\sqrt{\frac{k}{\mu}} \quad (1)$$

where c is the speed of light and μ is the reduced mass $\mu = \frac{m_1 m_2}{m_1 + m_2}$ of a diatomic molecule. m_1 and m_2 represent the masses of two atoms. k is the force constant of the molecular vibration. The constant k for a diatomic molecule depends exclusively on the electron cloud density, and the nuclear charge is independent of the mass; the k values for both H_2O and D_2O are identical. The relationship between the fundamental frequency vibrational absorption wavenumbers, denoted ν_1 and ν_2, for H_2O and D_2O can be expressed as follows[17]:

$$\frac{\nu_1}{\nu_2} = \sqrt{\frac{\mu_2}{\mu_1}} = 1.374 \quad (2)$$

where μ_1 and μ_2 represent the masses converted into masses of O−H and O−D, respectively. From the stretching vibration $\nu_{O\text{-}H} = 3400\ cm^{-1}$ and angular vibration $\nu'_{H\text{-}O\text{-}H} = 1640\ cm^{-1}$ of H_2O, the stretching vibration $\nu_{O\text{-}D} = 2470\ cm^{-1}$ and angular vibration $\nu'_{D\text{-}O\text{-}D} = 1194\ cm^{-1}$ of D_2O can be calculated. However, the actual molecule cannot be considered a harmonic oscillator. The quantum mechanical principles indicate that the nonharmonic oscillator can transition to higher energy levels, consequently resulting in the manifestation of double frequency peaks and sum frequency peaks. These transitions are inherently prohibited in the harmonic oscillator. Since the intensity of other high-frequency doubling peaks is too weak, we discuss the double frequency peak by doubling once.

Notably, D_2O, an isotope of water, is the second most abundant molecule on Earth, surpassed only by H_2O. Moreover, D_2O has been confirmed to be nontoxic and nonradioactive[18–21]. Unlike that of H_2O, the sum frequency absorption peak of D_2O does not fall within the NIR spectrum. Moreover, the amount of energy absorbed by the relaxation vibration of these two isotopes is intimately tied to the polarity of their respective chemical bonds under NIR radiation. According to Table S1 and S2, the polarity of D_2O molecules is lower than that of H_2O. This finding supports the conjecture in Fig. 1a that D_2O results in lower energy absorption than H_2O does under identical NIR radiation conditions, despite having the same molar mass.

Inspired by the aforementioned concept, we propose an ingenious approach to thermochromic smart windows using isotope-driven D_2O hydrogels, allowing for high visible light and entire solar spectrum transmittance ($\bar{T}_{Vis} = 92.99\%$ and $\bar{T}_{Sol} = 92.39\%$, intrinsic hydrogel $\bar{T}_{Vis} \approx 100\%$ and $\bar{T}_{Sol} = 99.8\%$ without encapsulation) at room temperature. Impressively, near-optimal modulation is achieved in the field of smart windows across the entire solar transmittance modulation ($\Delta T_{Sol} = 91.97\%$) and $\Delta T_{NIR} = 91.21\%$ in NIR, which is higher than that of conventional H_2O-hydrogel by an increase of ~16% in ΔT_{NIR}. Moreover, intrinsic hydrogel reflectance ($\Delta R_{Sol} = 86.73\%$ and $\Delta R_{NIR} = 81.57\%$) are notably superior to that of conventional H_2O-hydrogel, exhibiting an increase of ~19% in ΔR_{Sol} and ~31% in ΔR_{NIR}. The strong solar modulation facilitates an increase by 8.0 °C indoor cooling and 5.6 °C indoor heating in different modes. Additionally, further incorporating commercial Ag nanowires (Ag NWs) into D_2O hydrogels significantly enhances the regulation of longwave infrared (LWIR) emissivity ($\Delta\varepsilon_{LWIR} = 31.89\%$) while maintaining a comprehensive modulation ratio ($\Delta T_{Sol} = 66.02\%$, $\Delta R_{Sol} = 48.41\%$) that surpasses the capabilities of current thermochromic devices. Field experiment tracking and EnergyPlus simulation demonstrated that our isotope-driven D_2O hydrogel smart windows present substantial advantages in terms of energy conservation and CO_2 emission reduction across the majority of climatic zones globally. With the maturation of isotope separation and operational technologies, scaled-up production of D_2O hydrogels holds promising potential for next-generation smart window applications[22].

Results

Spectral variations induced by D_2O and H_2O

The experimental results in Fig. 1b and c indicate that the intrinsic NIR absorption of D_2O molecules is significantly weaker than that of H_2O (especially near the 1443 nm and 1926 nm bands) and that the absorption peak position closely aligns with the theoretically calculated value (approximately 1471 nm and 1984 nm). In addition, density functional theory (DFT) calculations further support these results (Tables S3–S5). Furthermore, both H_2O and D_2O demonstrate comparable absorption characteristics, with slight variations in intensity and peak position (Fig S1a), as well as high emissivity (Fig S1b), when the NIR wavelength range is replaced by longwave infrared (LWIR, 3–15 μm) range. We therefore employ H_2O and D_2O as solvents and N-isopropyl acrylamide (NIPAm) as the monomer to prepare four distinct hydrogels (HPN: PNIPAm hydrogels with H_2O as the solvent; HPN/PVA: HPN containing polyvinyl alcohol (PVA); DPN: PNIPAm hydrogels with D_2O as the solvent; and DPN/PVA: DPN containing PVA). As shown in Fig. 1d, both the DPN/PVA and DPN hydrogels display markedly superior transmittance to their HPN/PVA and HPN counterparts within the NIR wavelength range at room temperature (25 °C), whereas their reflectance values are comparable within the LWIR wavelength range. Remarkably, the DPN/PVA hydrogel (without encapsulation) demonstrates an intrinsic solar light transmittance of $\bar{T}_{Sol} = 99.8\%$ and a near-perfect visible light transmittance of $\bar{T}_{Vis} \approx 100\%$. The Density functional theoretical (DFT) results (Figs S2 and S3) reveal a significant difference between HPN and DPN systems within the spectral region of 2000-3000 cm^{-1}. Specifically, the symmetric and asymmetric stretching vibrations of O-H in the H_2O system occur exclusively above 3500 cm^{-1}, while the corresponding vibrations of O-D in the D_2O systems shift to 2500-3000 cm^{-1}. These observations confirm that the shift of infrared absorption peak of D_2O-based hydrogel, relative to H_2O-based hydrogel, is attributable to the D_2O solvent. We further investigated the influence of thickness on the solar transmittance spectra at room temperature, and the results clearly revealed a positive correlation (Figs S4 and S5). The spectral characteristics and versatility of various water isotope-driven hydrogels have been validated (Supplementary Information, Note S1 and Fig S6).

Figure 1e shows a photograph of the DPN/PVA hydrogels, featuring a D_2O content reaching 81.44% and a distinctive transparent appearance. As shown in Fig S7a, we employed two pieces of silica glass to encapsulate the DPN/PVA hydrogel. The macroscopic and microscopic schematic diagrams (Fig S7b) show that when the temperature falls below the lower critical solution temperature (LCST), the PNIPAm and PVA molecule chains dissolve seamlessly in D_2O, yielding a highly transparent and homogeneous hydrogel phase. Notably, the refractive index (n, $n = 1.364$) of this phase aligns closely with the intrinsic refractive index of D_2O ($n = 1.328$) under sodium yellow light at a wavelength of 589 nm. When the temperature exceeds the LCST, the intricate network undergoes a discernible phase transition, causing the intertwined chains of PNIPAm and PVA to collapse into hydrophobic microdomains that scatter light. As a result, the DPN/PVA smart window transforms into a translucent or completely opaque state. Furthermore, the LCST of both H_2O- and D_2O-based hydrogels is approximately 32 °C (Fig S8). The position of the peak attributed to the stretching vibrations of D−O (near 2461 cm^{-1}) is distinctly different from that of H−O (approximately 3297 cm^{-1}), as evidenced by the Fourier transform infrared (FTIR) and Raman spectroscopy results in Fig. 1f and g. Figure 1h reveal that the D_2O hydrogels have narrow absorption wavelength ranges than the H_2O hydrogels have within the NIR spectral range.

https://doi.org/10.1038/s41467-025-62432-3

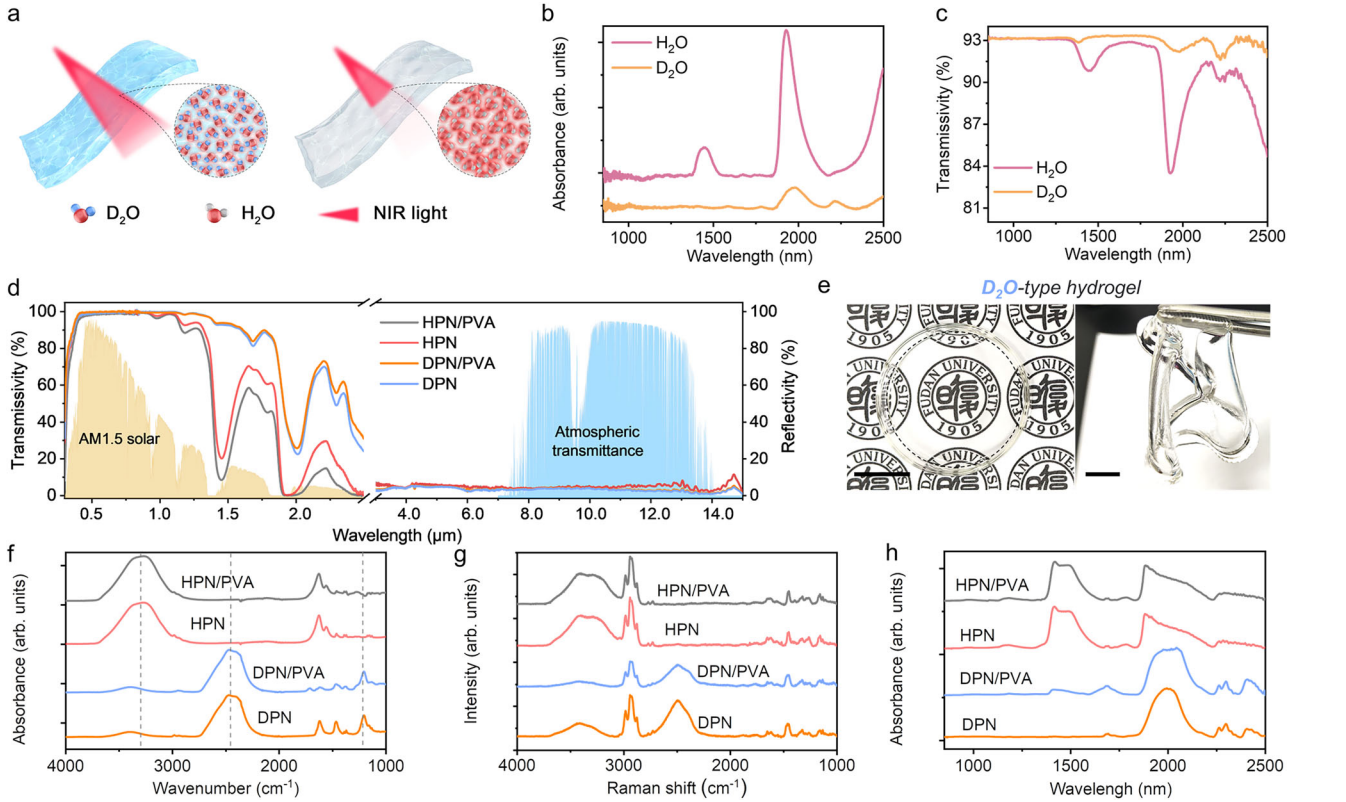

Fig. 1 | Differences in the spectra of H_2O and D_2O under near-infrared (NIR) light. a Schematic illustration of Near infrared (NIR) light passing through H_2O molecules and D_2O molecules. **b** NIR absorption spectra of H_2O and D_2O at 850–2500 nm. **c** NIR transmission spectra of H_2O and D_2O (sandwiched between double 1mm-silica glasses) at 850-2500 nm. **d** Measured transmissivity (ranging from 0.3 - 2.5 μm) and reflectivity (ranging from 3-15 μm) spectra of four types of gels (1 mm of thickness) plotted against the normalized ASTM G173 global solar spectrum and the atmospheric transparency window (ATW). **e** Image (a 2 cm scale ruler on the left and a 1 cm ruler on the right) of D_2O hydrogels (DPN/PVA). **f** FTIR absorbance spectrum, **g** Raman spectrum and **h** NIR absorption spectrum.

Fabrication and mechanism of isotope-driven hydrogel smart windows

As shown in Fig. 2a, the innovative D_2O hydrogels were encapsulated between two silica glass layers through either UV-curable or thermally initiated polymerization processes. Upon achieving thermal equilibrium with the external ambient temperature, the smart windows highly transmit (T < LCST) or effectively reflect (T > LCST) NIR and visible light. As a result, the smart window serves as a commonly employed thermal management solution, adaptively transmitting or reflecting the maximum possible amount of visible and NIR light (Fig. 2b). Surprisingly, as measured in Fig. 2c and d, the 1 mm thick DPN/PVA smart window achieves a respectable solar light transmittance ($\bar{T}_{Sol}$) of 92.39% and a significant NIR light transmittance ($\bar{T}_{NIR}$) of 92.14% at room temperature, allowing for a notable solar light modulation ratio (ΔT_{NIR}) of 91.36% during the cooling and heating cycles. In contrast, the $\bar{T}_{NIR}$ and ΔT_{NIR} values of the other three types of hydrogel smart windows are 81.59% and 80.73% for HPN/PVA, 82.05% and 78.52% for HPN, and 92.14% and 90.19% for DPN, respectively. To elucidate the mechanistic basis of temperature-driven spectral modulation in D_2O and H_2O systems, molecular dynamics (MD) simulations were employed as an effective comparative tool. The results of MD simulations (Figs S10–15) illustrate the variation of hydrogen bonds of four hydrogel systems. As temperature rises, the total number of hydrogen bonds in the system gradually diminishes (Fig S14). Furthermore, the decrease in hydrogen bonds numbers is less pronounced in the D_2O system compared to the H_2O system as temperature escalates, which may be attributed to the inherently weaker hydrogen bonds in H_2O relative to those in D_2O[23,24]. This transition causes the phase separation between PNIPAm chains and the aqueous medium, thereby facilitating the formation of a porous polymer network. The resulting light-scattering network manifests macroscopic whiteness by efficiently reflecting solar radiation across a broad spectrum, including the visible and near-infrared regions. After that, we quantified the maximum modulation ratios of visible light (ΔT_{Vis}) and solar light (ΔT_{Sol}) for four types of hydrogel smart windows with a thickness of 1 mm. As depicted in Fig S16 and S17, the ratios were as follows: 91.45% and 86.48% for HPN/PVA, 93.02% and 86.25% for HPN, 92.99% and 91.97% for DPN/PVA, and 92.86% and 91.40% for DPN. Promisingly, the DPN/PVA hydrogel smart window presented decent temporal stability, with a variation in transmittance of less than 1% at temperatures below 25 °C after 90 days of continuous transmittance testing (Fig. 2e). Furthermore, upon undergoing 200 cycles of heating and cooling, the transmittance modulation ability of isotope hydrogel (DPN/PVA) smart window remains above 90%, demonstrating its competent cycle durability (Fig S18). In response to climate resilience concerns, we have conducted accelerated aging tests that mimic extreme environmental conditions (Blackboard temperature of (60 ± 3) °C and irradiance of 0.68 W/m^2 with UV-A 340 nm and UV-B 313 nm, as detailed in Supplementary Information-Test method for aging resistance). The accelerated thermal aging process (50–60 °C, 256 h) reveals that critical phase separation-induced bubbles formation is more pronounced in hydrogels without PVA (Fig S19a), directly correlating with a loss in visible light transmittance (380–780 nm) versus PVA-stabilized systems (Figs S19b and Fig S20). Combined with Molecular dynamics (MD) simulations (Fig S14 and S15), these results suggest that the presence of a denser and stronger hydrogen bond network within the sample system, which includes PVA polymer chains, contributes to enhanced resilience against high temperatures and UV radiation.

Furthermore, we have categorized and compared state-of-the-art smart window technologies[1–3,7,10,11,25–50] (Table S6 and Fig. 2f). It is

https://doi.org/10.1038/s41467-025-62432-3

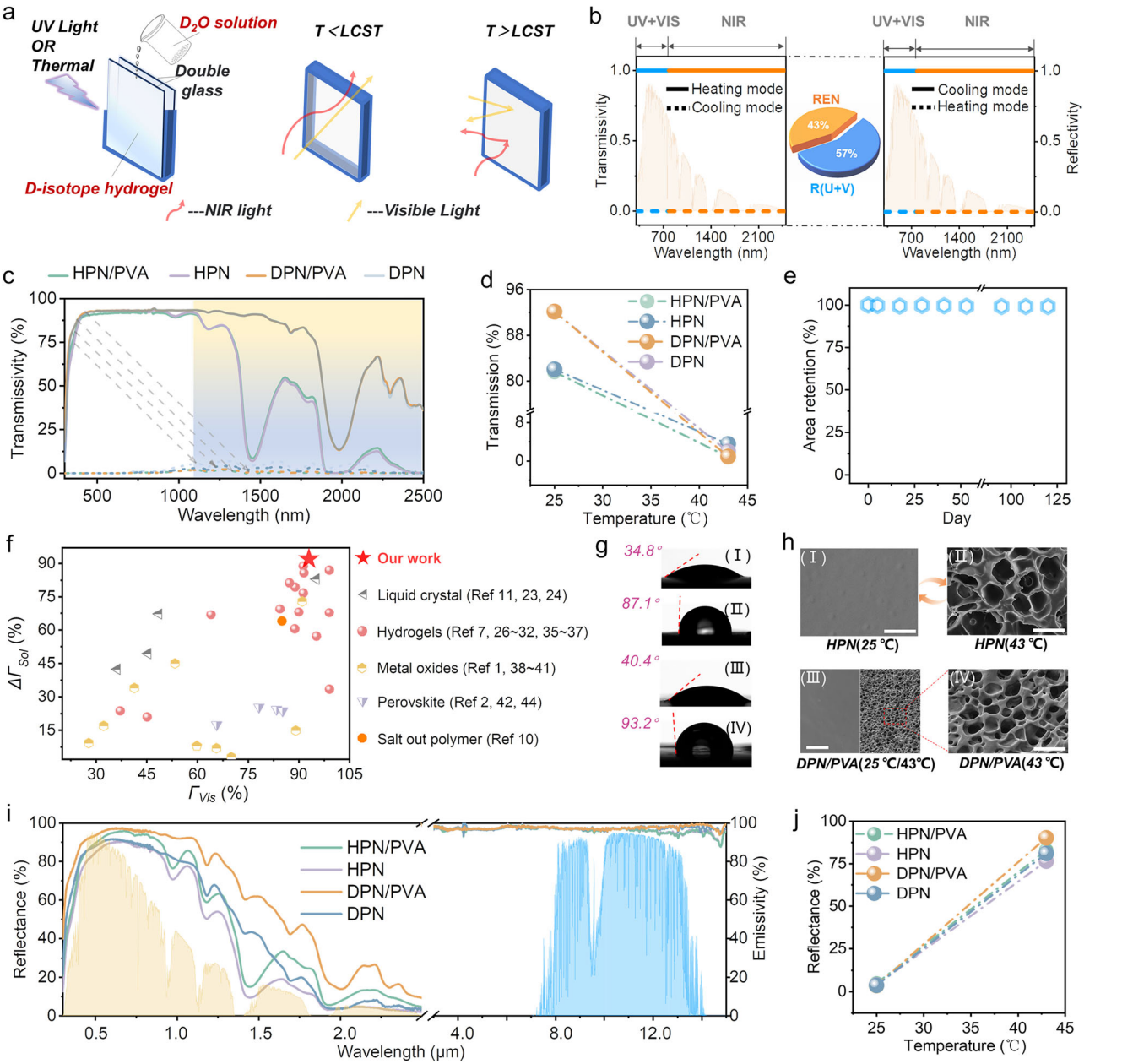

Fig. 2 | Characterization of the D_2O hydrogel smart windows. a Schematic of the preparation and regulation of the hydrogel smart windows. **b** Mechanism (enhancing the transmittance or reducing the reflectance in heating mode and enhancing the reflectance or reducing the transmittance in cooling mode; REN represents the NIR energy ratio, and RE(U + V) represents the UV and visible light energy ratio) by which ideal smart windows operate in a certain spectral range (0.3–2.5 μm). **c** Solar light transmittance spectra (ranging from 0.3–2.5 μm) at 25 °C (T < LCST) and 43 °C (T > LCST) for four types of hydrogel smart windows (the top of the image represents the solar light transmittance of four types of hydrogel smart windows at 25 °C). **d** Maximum modulation rate of NIR light transmittance at 25 °C and 43 °C. **e** Temporal (90 days) stability of the solar transmittance of the DPN/PVA smart window at 25 °C. **f** Classification and performance comparison of smart window field[1–3,7,10,22–48]. **g** Surface contact angles of (I) DPN/PVA at 25 °C and (II) at 43 °C; (III) HPN at 25 °C and (IV) at 43 °C. **h** Cross-sectional SEM images of (I) HPN at 25 °C, (II) HPN at 43 °C, and (III) DPN/PVA at 43 °C (right)/25 °C (left) and (IV)magnification of the local area of DPN/PVA at 43 °C (the 3 μm of white scale rulers correspond to I, II and IV; the 10 μm ruler corresponds to III). **i** Reflectance (ranging from 0.3–2.5 μm) and emissivity (ranging from 3–15 μm) spectra of four types of hydrogels plotted against the global solar spectrum and ATW. **j**) Maximum modulation ratio of the solar light reflectance at 25 °C and 43 °C.

noteworthy that D_2O-based hydrogels exhibit superior modulation ability due to the improvement in the NIR band.

Additionally, compared to nanostructured coatings (e.g., VO_2-based or plasmonic designs), D_2O-based hydrogels offer distinct advantages in the solar light modulation ($\Delta\Gamma_{Sol}$). Our investigations further reveal that the D_2O hydrogel smart windows, irrespective of encapsulation within silica glass (Fig S21a) or within commercial green glass (Fig S21b), display an approximately enhancement of 6% in visible light transmittance. This phenomenon of antireflection can be attributed to the distinct behavior of the visible light path within the hydrogel medium layer and air medium layer (Fig S21c). Additionally, the assessment of the haze (%) value post-encapsulation is absolutely important to ensure optimal performance in modern architecture. Pursuant to ASTM D1003, the formula used to calculate haze and its measurement method are shown in Eq. S3 and Note S2 (Fig S22).

Given the thermal management behavior of energy transmission through windows, the entire solar spectrum (0.3–2.5 μm) at room temperature should be considered. The shading coefficient (S_c) and

solar heat gain coefficient (*SHGC*) are considered important metrics for evaluating the thermal management efficacy[51], and the mathematical formulations used to calculate these coefficients are detailed in Eqs. S4 and S5, respectively. Accordingly, the corresponding results for the cooling/heating mode illustrate the notable ability of isotope D-type hydrogels to achieve solar energy shading (Fig S23). Given the rapid urbanization and increasing demand for cooling energy[2,52], the mechanism and efficiency of switchable smart windows have garnered considerable attention.

Figure 2g clearly shows that the DPN/PVA hydrogels undergo an obvious transformation from hydrophilic homogeneous networks (I, water contact angle (CA) = 34.8° at 25 °C) to more hydrophobic microdomains (II, CA = 87.1° at 43 °C), with CAs that differ from that of 93.2° (IV) for HPN at 43 °C (III, CA = 40.4° at 25 °C), allowing the smart windows to spontaneously switch without external energy, which can realize intelligent reversible adjustments tailored to the thermal management requirements. Figure 2h also confirms this point (I and II represent HPN images before and after the phase transition, respectively; III and IV represent the DPN/PVA SEM images). Notably, the cross-sectional SEM images of DPN/PVA at 43 °C show that the majority of the pore sizes are concentrated within the range of 0-2 μm, corresponding to the sunlight wavelength range of 0.3-2.5 μm (Fig. 2h-IV and Fig S24). In particular, the prevalence of nanopores in this distribution is conducive to enhancing the scattering of visible light wavelengths[7,53]. Combined with Fig. 2h and Fig S14, it is evident that D_2O systems display a higher density of hydrogen bonds and stronger intermolecular hydrogen bonding compared to H_2O systems. This difference arises from an increased prevalence of solvent-solvent interactions ("water-water" in Table S7), thereby a more substantial force is required to disrupt the cohesive hydrogen-bonding network of the entire system. Notably, the hydrogen bonds in D_2O systems show diminished reduction with increasing temperature (Fig S14), consistent with the results simulated by Radial Distribution Function (RDF, Fig S15). Intriguingly, D_2O systems form fewer hydrogen bonds between PNIPAm molecular chains and solvent molecules compared with H_2O systems (Table S7), potentially influencing the phase separation behavior. Specifically, the reduced bonding probability increases chain conformational flexibility, promoting the formation of smaller, interconnected pores through chain coiling and entanglement. Conversely, H_2O systems demonstrate enhanced polymer-solvent interactions, favoring collapse into larger, contiguous pores through cohesive network stabilization.

Importantly, the superiority of the D_2O-based isotopic mixture in terms of thermal regulation can be clearly embodied through the precise measurement of the reflectance ($\bar{R}_{Sol}$, 0.3–2.5 μm) and emissivity ($\bar{\varepsilon}1_{LWIR}$, 3–15 μm) spectra because the D_2O-based isotopic mixture absorbs less light than does the H_2O-based isotopic mixture (Fig. 2i). In the scenario wherein the DPN/PVA hydrogel smart window exclusively relies on the its intrinsic phase transition, without the incorporation of any additives or microstructure processing, the DPN/PVA hydrogel smart window attains an impressive $\bar{R}_{Sol}$ of 90.28% and a selective emissivity of 97.20% ($\bar{\varepsilon}2_{LWIR}$, 8–13 μm) at 43 °C on a par with ultra-white cooling materials nearly, significantly outperforming the other three smart windows. The COMSOL finite element results reveal that the simulated reflectivity spectra of four hydrogels at 43 °C (Fig S25) exhibit a highly consistent trend with the experimental observations (Fig. 2i), suggesting that the incorporation of PVA significantly enhances the solar reflectance of the hydrogel. Moreover, the incorporation of PVA molecular chains can increase the hydrophilicity of PNIPAm molecules, which not only facilitates water retention but also increases hydrogen bond formation between PNIPAm molecular chains (Fig S26). The phase separation of the PVA-containing hydrogel results in smoother holes and a more rounded perimeter, which differ from the jagged edges of the HPN pores and the elongated shape of the DPN pores (Fig S27). Compared to DPN, the DPN/PVA with a multistage pore distribution exhibits a more robust electric field distribution at 500 nm (Fig S28a), particularly at the interface between pores and polymers. This suggests the presence of significant impedance mismatches and scattering units at these interfaces, contributing to increased solar reflectance. In addition, the phenomenon observed in HPN/PVA is analogous to that in HPN. The large pore size and small porosity in HPN/PVA result in diminished interaction with sunlight at 500 nm (Figs S27 and S28a). When comparing DPN/PVA with HPN/PVA, the electric field intensity distribution (Fig S28b) of the H_2O-based systems is weaker, primarily due to the stronger absorption effect of H_2O than D_2O at 1500 nm. In addition, we further identified the optimal processing conditions for the PVA-containing hydrogel smart window, as illustrated in Fig S29.

To further evaluate the use of the hydrogels as smart windows for transitioning between heating and cooling modes, we also supplemented the solar reflectance $\bar{R}_{Sol}$ (Fig S30a, 4.77% for HPN/PVA, 3.89% for HPN, 3.55% for DPN/PVA, and 3.64% for DPN at low temperatures ≤ 25 °C) and $\bar{\varepsilon}2_{LWIR}$ in the 8–13 μm range at different angles (Fig S30b) for the DPN/PVA hydrogel smart window at room temperature. Encouragingly, as shown in Fig. 2k, the solar reflection modulation ratio (ΔR_{Sol}) is as high as 86.73% for DPN/PVA, which is obviously superior to 72.56% for HPN. Furthermore, Fig S31 shows the competent performance of the DPN/PVA hydrogel, with the maximum solar reflectance modulation ratio and high ΔR_{Vis} and ΔR_{NIR} values. Notably, the ΔR_{NIR} of DPN/PVA is significantly higher than common H_2O-hydrogel (HPN) by approximately 31%. The D_2O-based hydrogels are competitive with the latest composite materials, which rely on cutting-edge technologies, such as droplet template method, spraying deposition and 3D lithography, in terms of solar reflectance modulation ratio (ΔR_{Sol}) (Table S8). Additionally, an often unstated yet critical practical requirement for thermochromic devices is their compatibility with various colors. Currently, incorporating either inorganic colorants (metals[54], metal oxides[54–57], metal salts[54,57–59], etc.) or organic color paste (resin coatings of azo compounds[56], phthalocyanine[7,60,61] etc.) as additives inevitably leads to a decrease in cooling efficiency because of the high energy ratio of visible light (Fig. 2b). To harmonize the interplay between color and solar reflectance, we incorporated commercial discoloration microcapsules (DMs, ~32 °C of phase transition temperature, Fig S35) for the construction of rooftops and walls in buildings, which can switch between various colors and white according to temporal and spatial dimensions in diverse scenarios. The results show that the DPN/PVA extended to eight colors still possesses 65-75% entire solar modulation ΔR_{Sol} values.

Evaluation of the thermal management of isotope-driven hydrogel smart windows

Figure 3a shows that most individuals perceive the positioning of intelligent windows as a decisive factor in determining their radiative surface with a zenith direction of approximately 90°, which involves the aggravation of energy exchange between buildings and the ground or urban infrastructure (other radiative sources) with high temperatures, leading to heat waves hitting the modern building environment[62]. As depicted in Fig. 3b, the windows serve as modern building elements and maintain lower temperature than walls and grounds at different times of sunny summer days (Fig S36), directly leading to a challenge regarding the sub-environment cooling, which is expected to be solved with DPN/PVA hydrogels (Fig S37). To mitigate the secondary radiation caused by the heat gain effect, achieving passive subambient cooling using the coldness of the universe as the energy source through the atmospheric transparency window of 8–13 μm is imperative. The selective ratio (Y) is an important index of the utilization rate of ATW ($Y=\bar{\varepsilon}2_{LWIR}/\bar{\varepsilon}1_{LWIR}$). The modification of silica glass (SG) results in an increase to Y=1.02 from the Y=0.86 for the original smart windows (Fig. 3c), indicating an application for mitigating the heat island effect caused by urbanization. In addition, in

https://doi.org/10.1038/s41467-025-62432-3

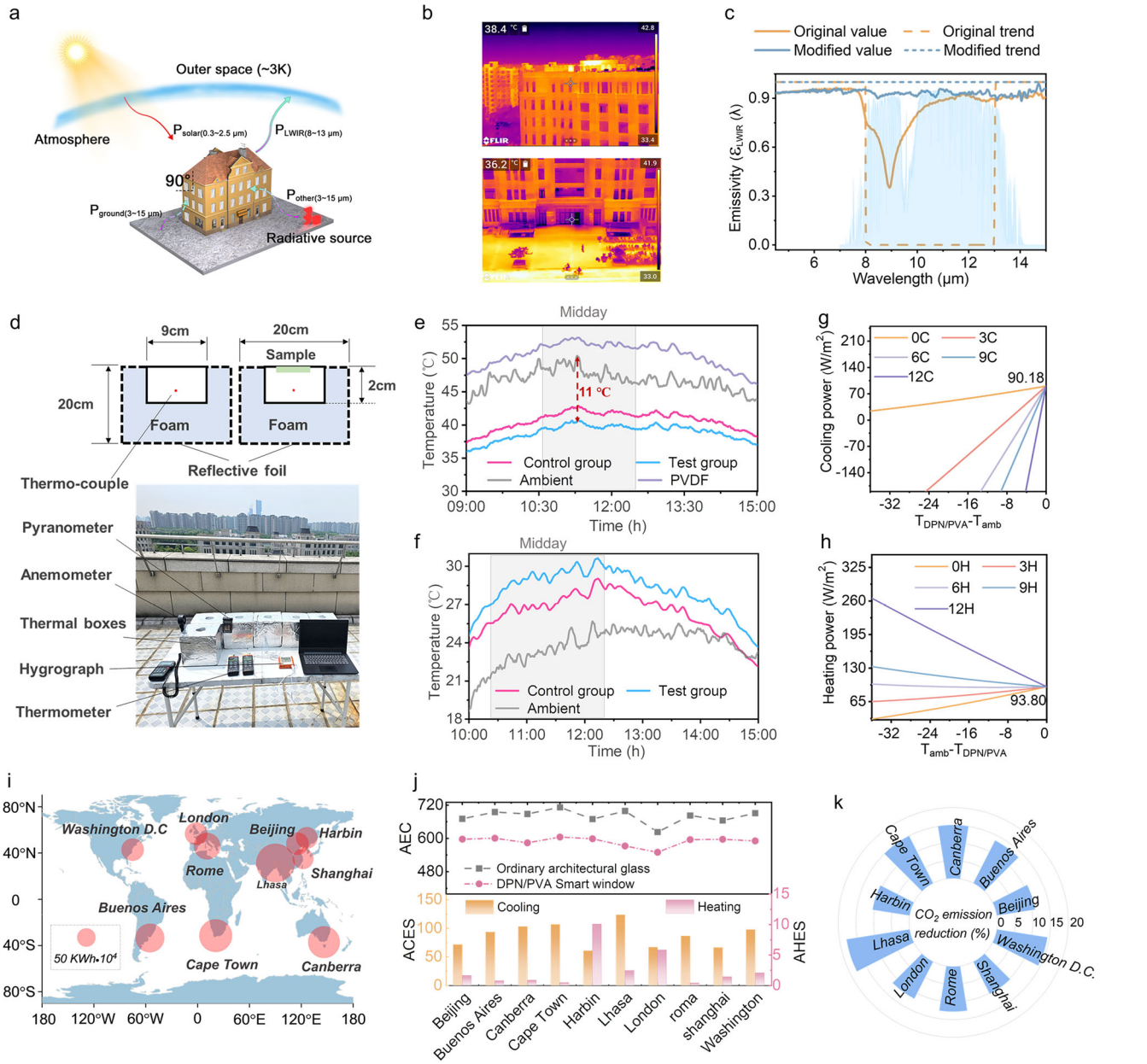

Fig. 3 | Evaluation of the thermal management of the D-type intelligent window combined with the actual scene. a Schematic of buildings in an actual scene. **b** Infrared thermal images of the architecture at different angles from 18:00–18:15 on July 9th, 2024, in Shanghai, China. **c)** LWIR spectral characteristics of architectural glass before and after modification. **d** Schematic and photograph of outdoor temperature-measuring devices. **e** Tracking the outdoor cooling temperature of the air and samples (control group: HPN smart window, test group: DPN/PVA smart window and PVDF film) on September 8th, 2023. **f** Tracking the outdoor heating temperature of the air and samples (control group: HPN smart window and test group: DPN/PVA smart window) on November 27th, 2023. The thickness of the hydrogel layer in both e) and f) is 3.4 mm. **g**, **h** represent calculated net radiative cooling (0 C: 0 W/m²/K + 9.72%P_{sun}; 3 C: 3 W/m²/K + 9.72%P_{sun}; 6 C: 6 W/m²/K + 9.72%P_{sun}; 9 C: 9 W/m²/K + 9.72%P_{sun}; 12 C: 12 W/m²/K + 9.72%P_{sun}) and heating (0H: 0 W/m²/K-7.51%P_{sun}; 3H: 3 W/m²/K-7.51%P_{sun}; 6H: 6 W/m²/K-7.51%P_{sun}; 9H: 9 W/m²/K-7.51%P_{sun}; 12H: 12 W/m²/K-7.51%P_{sun}) power of DPN/PVA smart windows. **i** Maps of 10 urban areas of different latitudes and longitudes on a world map and the annual energy savings compared with those of ordinary architectural glass. **j** Energy consumption and cooling and heating energy savings of the DPN/PVA smart window per year corresponding to each city (AEC: annual energy consumption; ACES: annual cooling energy savings; AHES: annual heating energy savings. All units are kWh·10⁴). **k** Carbon dioxide (CO_2) emission reduction (%) in 10 urban areas compared with that of ordinary architectural glass.

regard to smart windows of the hydrogel type, window-type hard encapsulation is a commonly considered solution because of the inherent water loss associated with high water content. In designing these encapsulation materials, it is important to balance both high transmission and emission properties across various modes.

The solar spectra of several organic polymers and inorganic glasses with identical thicknesses of 1 mm were determined (Fig S38a). We found that SG, when coated with either a layer of polyvinylidene fluoride (PVDF) or a specific PVDF-based polymer (poly(vinylidene difluoro-co-hexafluoropropylene), P[VDF-HFP]), i.e., PVDF@SG or PVDF-HFP@SG, exhibited pronounced absorption peaks at 8–13 μm (Fig S38b). Furthermore, without affecting the high transmittance of the encapsulation material (Fig S38c), the LWIR emissivity values $\bar{\varepsilon}1_{LWIR}$ and $\bar{\varepsilon}2_{LWIR}$ (Fig S38d) are higher than those of the original silica glass, which largely improves the resonant interactions of phonons and polarons in conventional SiO_2 materials. The contact angle (CA) of the modified surface shifted from 21.9° to 91.0° (Fig S38e and f). The spectral analysis (0.3–15 μm) of DPN/PVA encapsulated by the

PVDF@SG smart window is shown in Fig S38g. Compared with those of the SG (Fig S39a), the peaks of the refractive index (n) and extinction coefficient (κ) are blueshifted towards 8–13 μm (Fig S39b). With respect to the modification of the SG surface, not only does the transmittance remain unchanged (Fig S38c), but the increase in haze value is also inconspicuous (Fig S22f). The haze value of DPN/$PVA_{PVDF@SG}$ (smart window of DPN/PVA encapsulated by PVDF@SG) slightly increased to 1.67%. The encapsulation coatings of smart windows also possess mechanically robust (Note S4 and Figs S40–42).

A spacious rooftop that is close to an area with minimal building obstruction was selected, ensuring optimal exposure to sunlight in Shanghai, China (31°20′24″ N, 121°31′12″ E), and a custom-made experimental setup and a series of subambient tracking devices, including thermocouples, thermal boxes, hygrographs, anemometers, thermometers, pyranometers, etc., were built (Fig. 3d or Fig S43). Fig S44 depicts the fluctuations in solar irradiance at certain temporal intervals. Furthermore, Figs. 3e, f present two modes of cooling and heating, respectively, and the corresponding wind speed and humidity data are shown in Fig S45. As shown in Fig S46a, the rooftop peak temperature approached 50 °C, and the smart window immediately starts in the cooling mode, resulting in a discernible decrease in temperature compared with both the ambient and PVDF resin films during intense irradiation and hot days. Moreover, the relative humidity, wind speed, and solar irradiance were also recorded at the corresponding moments in Figs S46b and c. We further calculated the average difference ($\Delta T=T_{ambient}-T_{groups}$, $T_{ambient}$: average ambient temperature; T_{groups}: average temperature of control group, test group and PVDF film) between the ambient temperature and temperature of groups (control group: $\Delta T_1 = 5.9$ °C, test group: $\Delta T_2 = 8.0$ °C, and PVDF film: $\Delta T_3 = -4.5$ °C) at a mean irradiation intensity of 916 W/m² (Figs. 3e and S44a), a mean wind speed of 0.9 m/s and a humidity of 43.0%, as shown in Fig S45a. It is worth mentioning that the maximum difference between environment and test group was as high as ~11 °C. In addition, the cooling assessment along with the corresponding monitoring, which incorporates distinct DMs, such as malachite green, dark blue, and peach–red, was successfully validated (Note S5 and Fig S47).

Similarly, we maintained virtually identical experimental setups at the same location but under different climatic conditions, with a peak ambient temperature of approximately 25 °C (Figs S48 and S49). Under these conditions, we tracked the midday temperature performance of the smart window in this heating mode as illustrated in Figs. 3f, S44b and S45b, demonstrating a relatively notable temperature difference: $\Delta T_1 = -3.7$ °C (control group) and $\Delta T_2 = -5.6$ °C (test group) at an average irradiation intensity of 674 W/m², a mean wind speed of 1.2 m/s and a humidity of 40.5%. To align the position of the devices with real-world building windows and simulate varying sunlight conditions across different weather scenarios, the sample devices were positioned at 0° and 90° relative to the horizontal plane, respectively, in Shanghai (31°20′24″N, 121°31′12″E) (Note S6 and Figs. S50–S53). Figures 3g, h present the theoretical predictions for the radiative thermal management of DPN/PVA smart windows in heating mode (25 °C) and cooling mode (43 °C), respectively, via MATLAB[63,64], revealing a noteworthy cooling power of 90.18 W/m² and a heating power of 93.80 W/m² at a uniform solar irradiance of 500 W/m², which are considerably superior to the theoretical cooling and heating powers of other hydrogel smart windows (Figs S54 and S55). To better simulate and verify the cooling efficacy of D-type hydrogel smart windows under conditions where radiation is the sole heat transfer factor, we further measured where the adiabatic incubator was sealed with a highly transparent low-density polyethylene (LDPE) film of ~10 μm thickness (Fig. S56 and S57).

To evaluate the energy-saving potential of this innovative isotope-driven hydrogel smart window more intuitively, we randomly selected ten cities worldwide, each with varying latitudes and longitudes, as depicted in Fig. 3i. EnergyPlus software was used to calculate the annual energy savings achieved by the smart windows when they were utilized as office building windows. Benefiting from the dual contributions of the dynamic cooling and heating capabilities, the DPN/PVA smart window achieves obvious energy savings of approximately 90.27 kWh×10⁴, outperforming conventional architectural glass (Figs. 3i, j). Moreover, the annual energy savings of four hydrogel smart windows in these ten cities reveal that the DPN/PVA hydrogel smart window has a distinct advantage in terms of energy conservation (Fig S58). Despite ongoing challenges related to cost-effectiveness and scalability for commercial expansion of D_2O-based hydrogels, these hydrogels demonstrate a more pronounced energy-saving benefit compared to those based on H_2O. In terms of environmental protection, compared with conventional building glass, D-type smart windows effectively decrease CO_2 emissions in each city by more than 10% (Fig. 3k).

Synchronous solar and thermal radiation regulation of isotope-driven hydrogel smart windows

Despite the extensive modulation of solar light based on the microenvironment of the D_2O isotope and the phase separation mechanism of PNIPAm hydrogels, there remains a limitation in extending this modulation seamlessly to LWIR (especially at 8–13 μm) owing to the phonon polaron resonance of the encapsulated silica glass[63,65]. Thus, we selected commercial polyethylene (PE) plastic wrap as the encapsulation material owing to its high transmittance of solar light (Fig S59a) and LWIR (Fig S59b), which not only satisfies the regulation mechanism required for D-type hydrogels under sunlight but also presents a promising avenue for modulating the material's response within the 8–13 μm wavelength range. The use of PE plastic wrap as an encapsulation film for hydrogels results in a water contact angle of 88.1°, ensuring greater stability than that of hydrogels alone (Fig S59c). As illustrated in Figs S59d and e, the comprehensive spectrum of DPN/PVA postencapsulation maintains high sunlight transmittance and a large modulation ratio ($\Delta\Gamma_{Sol} = 90.35\%$), which is essentially unaffected by PE packaging. The refractive index (n), extinction coefficient (κ), and haze (%) performance of the PE plastic wrap are illustrated in Figs S22 and S60.

We subsequently selected commercial silver nanowires (Ag NWs) with a diameter of 20 nm (Fig S61) to encapsulate the assembled interface of the DPN/PVA hydrogel smart window because of their high solar transmission and strong LWIR reflection (Fig. 4a), and Ag@DPN/PVA_{PE} (AGD) smart windows were obtained. The detailed spectral modulation mechanism of AGD is discussed in detailed between Notes S7–S9 in Supplementary Information. It is necessary to comprehensively evaluate the modulation of both solar transmission/reflectance and LWIR emissivity to attain optimal performance (Fig. 4b–e and Figs S64–S66) for smart windows in real-world applications. Figure 4f shows the measured transmissivity (0.3–2.5 μm) and emissivity (3–15 μm) spectra of the AGD smart window at 25 °C and 43 °C, featuring a thickness achieved with spin-coating at 3000 rpm, suggesting the competitive regulation of LWIR emissivity ($\Delta\varepsilon_{LWIR} = 31.89\%$) and solar transmittance/ reflectance ($\Delta\Gamma_{Sol} = 66.02\%$/ $\Delta R_{Sol} = 48.41\%$). In terms of thermochromic comprehensive performance[1,3,4,66–78] with thermal emissivity modulation (Table S10 and Fig. 4g) in recent years, our AGD smart window continues to exhibit decent $\Delta\Gamma_{Sol}$, which is notably superior to the high-performance H_2O-hydrogel system ($\Delta\Gamma_{Sol} = 58.4\%$) reported so far.

Considering the inherent thermal conductivity and heat capacity of Ag NWs, commercial low-E glass was chosen as the benchmark for the outdoor test. We conducted outdoor tracking tests for both heating and cooling modes (Figs. 4h, i, S67 and S68). Compared with the commercially available low-E glass, the DPN/PVA_{PE} smart window, the 500 rpm AGD smart window, and the 3000 rpm AGD smart window demonstrate reductions of 16 °C, 5.8 °C and 9.2 °C, respectively (Fig. 4h and Fig S69a). The discrepancy between silica glass coated

https://doi.org/10.1038/s41467-025-62432-3

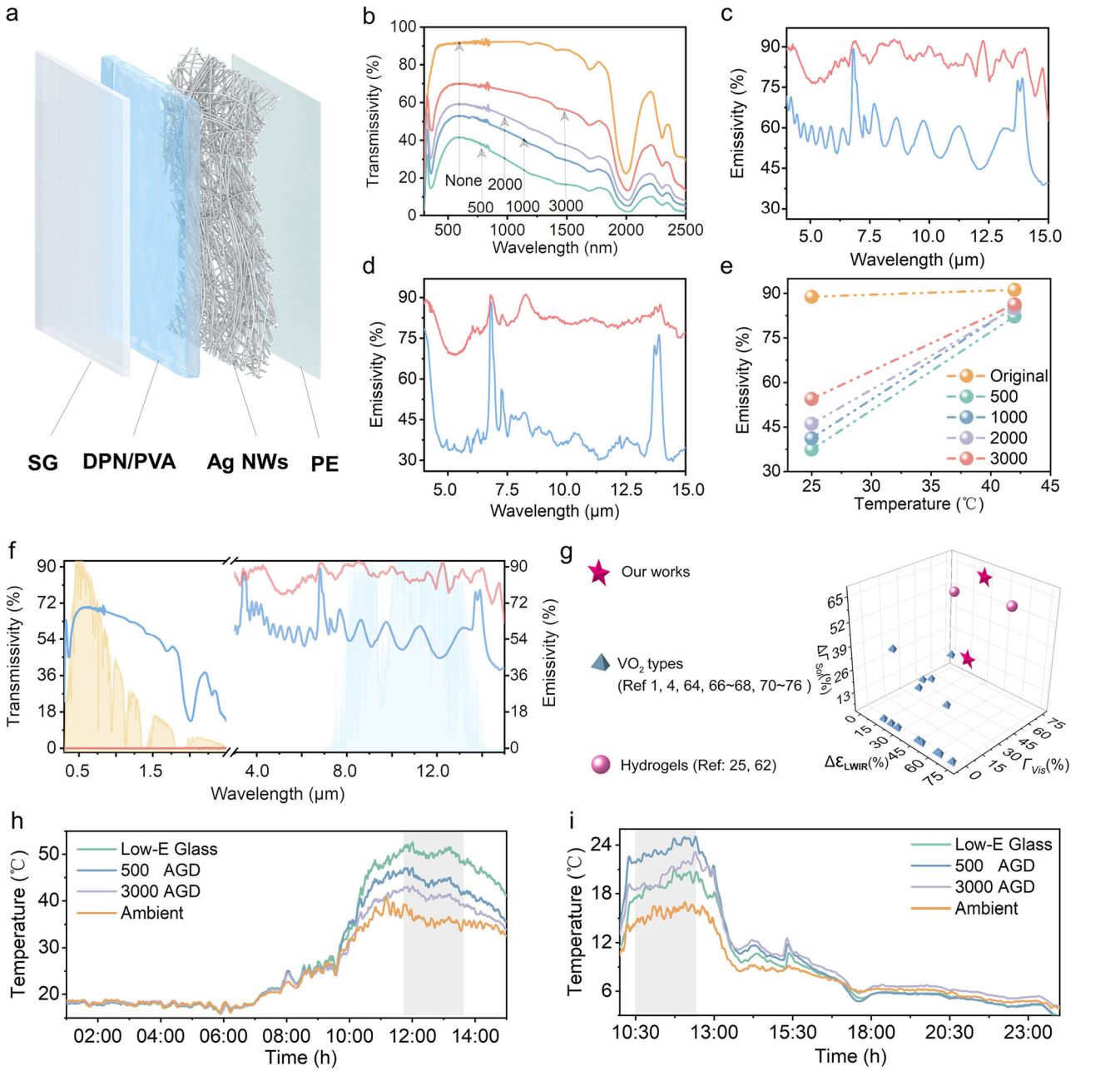

Fig. 4 | Intelligent window design with full-spectrum modulation capability. **a** Fabricated structure of D_2O-type smart windows. **b** Transmittance (measured at 0.3–2.5 μm) of DPN/PVA smart windows with layers of different Ag NWs thicknesses (none: without Ag NWs: 500: Ag NWs layer spin-coated at 500 rpm; 1000: Ag NWs layer spin-coated at 1000 rpm; 2000: Ag NWs layer spin-coated at 2000 rpm; 3000: Ag NWs layer spin-coated at 3000 rpm). **c**, **d** Emissivity of the 3000 and 500 DPN/PVA smart windows at 25 °C and 43 °C, respectively. **e** Maximum modulation ratio of the LWIR emissivity (8–13 μm, ATW) at 25 °C and 43 °C. **f** Measured transmissivity (ranging from 0.3–2.5 μm) and emissivity (ranging from 3–15 μm) spectra of the 3000 DPN/PVA smart window plotted against the global solar spectrum and ATW at 25 °C and 43 °C. **g** Comparison of thermochromic comprehensive performance[1,3,4,66–78] with thermal emissivity modulation ($\Delta\varepsilon_{LWIR}$). **h**, **i** Temperature records of the samples (low-E glass: commercial low-emissivity glass; 500 AGD: DPN/PVA smart window with an Ag NWs layer spin-coated at 500 rpm; 3000 AGD: DPN/PVA smart window with an Ag NWs layer spin-coated at 3000 rpm; Ambient: temperature of the air) at the corresponding temperatures on October 25h, 2023, and January 26th, 2024.

with Ag NWs at 3000 rpm and low-E glass is 1.3 °C in cooling mode (Fig S69a and Fig. 4h), underscoring the potential significance of radiation regulation in the AGD smart window.

As a complement, we performed a detailed optimization of the spin-coating speed parameter. To achieve a balance between the cooling effect and the LWIR thermal emissivity, we conducted outdoor tests to track the temperature variations of AGD smart windows with Ag NW layers spin-coated at 3000 rpm, 4000 rpm, and 5000 rpm (Fig S70). With respect to the ambient temperature, the $\Delta T_{3000\ AGD}$, $\Delta T_{4000\ AGD}$ and $\Delta T_{5000\ AGD}$ are all approximately 2.0 °C, and $\Delta T_{DPN/PVAPE}$ is approximately −4.1 °C at an average sunlight intensity of 641.75 W/m^2. Similarly, the AGD smart window exhibited better heat storage and heating performance than did commercial low-E glass in heating mode. From 10:30 to 12:30, at an average solar irradiation intensity of 604.29 W/m^2 and an average ambient temperature of 15.7 °C, the DPN/PVA_{PE} smart window experienced a decrease in temperature of 2.5 °C, whereas the 500 rpm and 3000 rpm AGD smart windows

experienced an increase in temperature of 4.2 °C and 1.1 °C, respectively, with the low-E glass window acting as a baseline (Figs S67b, S67b, S69b and Fig. 4i). To mitigate oxidation of Ag NWs, we implemented a multi-layer encapsulation strategy combining physical barrier engineering and material optimization in Supplementary information- Encapsulation of PE plastic wrap *vs*. BaF_2 glass (Note S10 and Figs S71–S75). The results indicate that AGD hydrogels encapsulated with BaF_2 glass possess a superior solar transmission modulation ratio ($\Delta\Gamma_{Sol}$ = 82%) and mid-infrared (8–13 μm) modulation ratio ($\Delta\varepsilon_{LWIR}$ = 34.15%) compared to those encapsulated with PE. When compared to commercial Low-E glass, the BaF_2-encapsulated AGD hydrogels can achieve an additional heating of approximately 3 °C (Fig S76). Importantly, future advancements in synthesis processes are anticipated to meet the important criteria for both miniaturization and pilot-scale production (Figs S78–S80).

Discussion

In summary, we designed novel isotope-driven D_2O hydrogel smart windows for high-performance thermoregulation, which effectively mitigates the inherent NIR energy absorption by traditional H_2O hydrogels. This remarkably innovative hydrogel smart window presents notable visible light transmittance ($\bar{\Gamma}_{Vis}$ = 92.99%, intrinsic hydrogel $\bar{\Gamma}_{Vis} \approx 100\%$ without encapsulation) at room temperature and a relatively high level of solar light modulation capacity ($\Delta\Gamma_{Sol}$ = 91.97% and ΔR_{Sol} = 86.73%) of current smart windows field during cooling and heating modes, thereby fulfilling the demands for dynamic energy management across diverse climate zones. Furthermore, the incorporation of commercial Ag NWs and encapsulation with PE plastic wrap can ensure the concurrent and effective modulation of both solar radiation and LWIR radiation. The versatile isotope D_2O hydrogel smart windows employed in modern architecture present substantial advantages in terms of energy conservation and CO_2 emission reduction. The limitation lies in the higher cost of D_2O due to isotope separation relative to conventional hydrogels, which may be reduced by ongoing investigations.

Methods

Fabrication of smart windows

First, 3.40 g (0.03 mol) of NIPAm was dissolved in 11 mL of D_2O at room temperature. Then, 4 mL of PVA solution (with D_2O as the solution, Supplementary Methods in Supplementary Information) was added, followed by mixing at 600 rpm for 30 min. After that, 0.0087 g of HHM (initiator), 0.0043 g of MBA (crosslinker), and 0.05-0.07 g of LiBr were added at the same time and ultrasonicated until they were completely dissolved. Finally, this solution was poured into a designated silica glass (7 cm × 7 cm, with the top of the encapsulation material being PVDF@SG/P(VDF-HFP)@SG mould Supplementary Methods in Supplementary Information), whose height depends on the surrounding silicone gasket, and the reaction was initiated in an ice bath for more than 40 min under ultraviolet light (365 nm, energy density of 120 μJ·cm^{-2}) in a N_2 atmosphere. By the way, the inner sides of the silicone gasket were previously immersed in benzophenone solution (22 wt% acetone) for 20 min. The DPN/PVA intelligent window was attained, and the DPN intelligent window can also be appropriate without a PVA solution. With the same molar ratio (NIPAm, PVA or D_2O), the corresponding smart windows (HPN/PVA or HPN) with H_2O as the solvent were prepared via the same method.

In addition to UV curing, it can also be prepared by thermal crosslinking, in which 6-10 mg of Na_2HSO_3 and 5 mg of APS were used instead of the previous HHM photoinitiator. If it is necessary to prepare colored hydrogel samples, color-changing microcapsules (with a monomer solid content of only 1 wt%) are added to the original system.

Preparation of Ag NWs—DPN/PVA (AGD) smart windows

The glass was cleaned with ethanol and water, dried, and treated with oxygen plasma (100 W, 5 min). The surface of the glass was then spin-coated with an Ag NWs dispersion and allowed to air dry. The side containing the Ag NWs coating can be used as the bottom encapsulating hydrogel prepolymer. The top was sealed with quartz glass. After 365 nm UV curing for more than 40 min, the bottom glass plate was removed and replaced with commercial PE plastic wrap (~15 μm) for encapsulation.

Data availability

All data are available from the corresponding author upon request.

References

1. Wang, S. et al. Scalable thermochromic smart windows with passive radiative cooling regulation. *Science* **374**, 1501–1504 (2021).
2. Liu, S. et al. Mask-inspired moisture-transmitting and durable thermochromic perovskite smart windows. *Nat. Commun.* **15**, 876 (2024).
3. Lin, C. et al. All-weather thermochromic windows for synchronous solar and thermal radiation regulation. *Sci. Adv.* **8**, eabn7359 https://doi.org/10.1126/sciadv.abn7359.
4. Tang, K. et al. Temperature-adaptive radiative coating for all-season household thermal regulation. *Science* **374**, 1504–1509 (2021).
5. Li, X. et al. Self-rolling of vanadium dioxide nanomembranes for enhanced multi-level solar modulation. *Nat. Commun.* **13**, 7819 (2022).
6. Li, T. et al. A radiative cooling structural material. *Science* **364**, 760–763 (2019).
7. Chen, G. et al. Printable Thermochromic Hydrogel-Based Smart Window for All-Weather Building Temperature Regulation in Diverse Climates. *Adv. Mater.* **35** https://doi.org/10.1002/adma.202211716 (2023).
8. Sui, C. et al. Dynamic electrochromism for all-season radiative thermoregulation. *Nat. Sustain.* **6**, 428–437 (2023).
9. Paulos, J. & Berardi, U. Optimizing the thermal performance of window frames through aerogel-enhancements. *Appl. Energ.* **266**, 114776 (2020).
10. Saju, S. K. et al. Thermochromic polymer blends. *Joule* https://doi.org/10.1016/j.joule.2024.07.020 (2024).
11. Deng, Y. et al. Annual energy-saving smart windows with actively controllable passive radiative cooling and multimode heating regulation. *Adv. Mater.* **36** https://doi.org/10.1002/adma.202401869 (2024).
12. Qin, Y. et al. Amplified positive effects on air quality, health, and renewable energy under China's carbon neutral target. *Nat. Geosci.* **17**, 411–418 (2024).
13. Hua, M. et al. Strong tough hydrogels via the synergy of freeze-casting and salting out. *Nature* **590**, 594–599 (2021).
14. Peña, J. J. et al. Position-dependent mass Schrödinger equations allowing harmonic oscillator (HO) eigenvalues. *Int. J. Quantum Chem.* **108**, 2906–2913 (2008).
15. Bukar, H. et al. Approximate Solution of Schrodinger Equation to Diatomic Molecule for Harmonic Oscillator. *UMYU Sci.* **2**, 028–036 (2023).
16. Barbosa, T. N. et al. A quantum Monte Carlo study of confined quantum systems: application to harmonic oscillator and hydrogenic-like atoms. *J. Phys. B-. Mol. Opt.* **48**, 055002 (2015).
17. Weng, S. *Fourier transform infrared spectroscopy analysis*, 2nd edn. (Beijing Chemical Industry Press, 2015).
18. Liu, J. et al. Application of deuterated compounds. *Deuteride Materials*, pp. 231–285. https://doi.org/10.1007/978-981-13-6962-9_6 (Singapore: Springer, 2019).
19. Atomic Energy Regulatory Board. Safety aspects in design and operation of heavy water plants. No. AERB/HWP/SG–1, pp. 14–20 (Atomic Energy Regulatory Board, Mumbai, 2014).

20. Mariano, M.dS. R. et al. Biotechnological Patents Applications of the Deuterium Oxide in Human Health. *Recent Pat. Biotechnol.* **11**, 76–84 (2017).
21. Tikhomirov, V. V. *Hydrogeochemistry Fundamentals and Advances, Groundwater Composition and Chemistry*. 1 (John Wiley & Sons, 2016).
22. Su, Y. et al. Separating water isotopologues using diffusion-regulatory porous materials. *Nature* **611**, 289–294 (2022).
23. Shin, M. J. et al. Reversible Chromatic response of polydiacetylene derivative vesicles in D_2O Solvent. *Langmuir* **32**, 882–888 (2016).
24. Stefaniuk, A. et al. Isotope effects observed in diluted D_2O/H_2O mixtures identify HOD-induced low-density structures in D_2O but not H_2O. *Sci. Rep.* **12**, 18732 (2022).
25. Li, B. et al. Self-Adhesive Self-Healing Thermochromic Ionogels for Smart Windows with Excellent Environmental and Mechanical Stability, Solar Modulation, and Antifogging Capabilities. *Adv. Mater.* **35** (2023). https://doi.org/10.1002/adma.202211456
26. Deng, Y. et al. Ultrafast Switchable Passive Radiative Cooling Smart Windows with Synergistic Optical Modulation. *Adv. Funct. Mater.* **33** https://doi.org/10.1002/adfm.202301319 (2023).
27. Liu, Y. et al. A Stable and Self-Healing Thermochromic Polymer Coating for All Weather Thermal Regulation. *Adv Funct Mater* **33** https://doi.org/10.1002/adfm.202307240 (2023).
28. Soo, X. Y. D. et al. Ultra-high Performance Thermochromic Polymers via a Solid-solid Phase Transition Mechanism and Their Applications. *Adv. Mater.* https://doi.org/10.1002/adma.202405430 (2024).
29. Wang, S. et al. A solar/radiative cooling dual-regulation smart window based on shape-morphing kirigami structures. *Mater. Horiz.* **10**, 4243–4250 (2023).
30. Zhang, Q. et al. Ultra-Compliant and Tough Thermochromic Polymer for Self-Regulated Smart Windows. *Adv. Funct. Mater.* **31** https://doi.org/10.1002/adfm.202100686 (2021).
31. Yu, Z. et al. Bidirectional optical response hydrogel with adjustable human comfort temperature for smart windows. *Mater. Horiz.* **11**, 207–216 (2024).
32. Wang, W. et al. Bidirectional temperature-responsive thermochromic hydrogels with adjustable light transmission interval for smart windows. *Adv. Funct. Mater.* https://doi.org/10.1002/adfm.202413102 (2024).
33. Xu, G. et al. Thermochromic Hydrogels with Dynamic Solar Modulation and Regulatable Critical Response Temperature for Energy-Saving Smart Windows. *Adv. Funct. Mater.* **32** https://doi.org/10.1002/adfm.202109597 (2021).
34. Li, J. et al. A Facile yet Versatile Strategy to Construct Liquid Hybrid Energy-Saving Windows for Strong Solar Modulation. *Adv. Sci.* **10** https://doi.org/10.1002/advs.202206044 (2023).
35. Zhou, Y. et al. Liquid thermo-responsive smart window derived from hydrogel. *Joule* **4**, 2458–2474 (2020).
36. Wang, M. et al. Electrochromic Smart Windows Can Achieve an Absolute Private State through Thermochromically Engineered Electrolyte. *Adv. Energy Mater.* **9** https://doi.org/10.1002/aenm.201900433 (2019).
37. Xie, L. et al. Engineering self-adaptive multi-response thermochromic hydrogel for energy-saving smart windows and wearable temperature-sensing. *Small* **19**, 2304321 (2023).
38. Li, X.-H. et al. Broadband Light Management with Thermochromic Hydrogel Microparticles for Smart Windows. *Joule* **3**, 290–302 (2019).
39. Wang, S. et al. Warm/cool-tone switchable thermochromic material for smart windows by orthogonally integrating properties of pillar[6]arene and ferrocene. *Nat. Commun.* **9**, 1737 (2018).
40. Shao, Z. et al. Tri-band electrochromic smart window for energy savings in buildings. *Nat. Sustain.* **7**, 796–803 (2024).
41. Sheng, S.-Z. et al. Nanowire-based smart windows combining electro- and thermochromics for dynamic regulation of solar radiation. *Nat. Commun.* **14**, 3231 (2023).
42. Meng, W. et al. Scalable photochromic film for solar heat and daylight management. *Adv. Mater.* **36**, 2304910 (2024).
43. Zhao, F. X. et al. Bio-inspired mechanically responsive smart windows for visible and near-infrared multiwavelength spectral modulation. *Adv. Mater.* https://doi.org/10.1002/adma.202408192 (2024).
44. Liu, S. et al. Near-Infrared-activated thermochromic perovskite smart windows. *Adv. Sci.* **9**, 2106090 (2022).
45. Lin, J. et al. Thermochromic halide perovskite solar cells. *Nat. Mater.* **17**, 261–267 (2018).
46. Liu, S. et al. Organic Hybrid Perovskite ($MAPbI_3$-Cl) for Thermochromic Smart Window with Strong Optical Regulation Ability, Low Transition Temperature, and Narrow Hysteresis Width. *Adv. Funct. Mater.* **31**, 2010426 (2021).
47. Chen, S. et al. Robust solvatochromic gels for self-defensive smart windows. *Adv. Funct. Mater.* **33**, 2214382 (2023).
48. Zhang, C. et al. Vapor–liquid transition-based broadband light modulation for self-adaptive thermal management. *Adv. Funct. Mater.* **32** https://doi.org/10.1002/adfm.202208144 (2022).
49. Chen, H. et al. Compression-sensitive smart windows: inclined pores for dynamic transparency changes. *Nat. Commun.* **15** https://doi.org/10.1038/s41467-024-52305-6 (2024).
50. Mandal, J. et al. Porous polymers with switchable optical transmittance for optical and thermal regulation. *Joule* **3**, 3088–3099 (2019).
51. Meng, W. et al. Photochromic thermoelectric smart window for season-adaptive solar heat and daylight management. *Adv. Funct. Mater.* **34**, 2402494 (2024).
52. Kato, F. et al. Unveiling two deuteration effects on hydrogen-bond breaking process of water isotopomers. *Phys. Rev. Mater.* **3**, 112001 (2019).
53. Mandal, J. et al. Hierarchically porous polymer coatings for highly efficient passive daytime radiative cooling. *Science* **362**, 315–319 (2018).
54. Li, J. et al. Printable, emissivity-adaptive and albedo-optimized covering for year-round energy saving. *Joule* **7**, 2552–2567 (2023).
55. Lin, K. et al. Hierarchically structured passive radiative cooling ceramic with high solar reflectivity. *Science* **382**, 691–697 (2023).
56. Peng, Y. et al. Colorful low-emissivity paints for space heating and cooling energy savings.*Proc. Natl. Acad. Sci.* **120**, e2300856120 (2023).
57. Cai, L. et al. Temperature regulation in colored infrared-transparent polyethylene textiles. *Joule* **3**, 1478–1486 (2019).
58. Xue, X. et al. Creating an eco-friendly building coating with smart subambient radiative cooling. *Adv. Mater.* **32**, 1906751 (2020).
59. Wang, X. et al. Sub-ambient full-color passive radiative cooling under sunlight based on efficient quantum-dot photoluminescence. *Sci. Bull.* **67**, 1874–1881 (2022).
60. Wu, X. et al. A dual-selective thermal emitter with enhanced subambient radiative cooling performance. *Nat. Commun.* **15**, 815 (2024).
61. Wang, Z. et al. Dual-tunable structural colors from liquid-infused aerogels. *Adv. Opt. Mater.* **8**, 1901825 (2020).
62. Wu, R. et al. Spectrally engineered textile for radiative cooling against urban heat islands. *Science* **384**, 1203–1212 (2024).
63. Mei, X. et al. A self-adaptive film for passive radiative cooling and solar heating regulation. *J. Mater. Chem. A* **10**, 11092–11100 (2022).
64. Wang, T. et al. A structural polymer for highly efficient all-day passive radiative cooling. *Nat. Commun.* **12**, 365 (2021).
65. Min, X. et al. A smart thermal-gated bilayer membrane for temperature-adaptive radiative cooling and solar heating. *Sci. Bull.* **68**, 2054–2062 (2023).

66. Du, J. et al. Enhancing thermochromic performance of VO_2 films via increased microroughness by phase separation. *Sol. Energ. Mat. Sol. C.* **110**, 1–7 (2013).
67. Kang, L. et al. Pt/VO_2 double-layered films combining thermochromic properties with low emissivity. *Sol. Energ. Mat. Sol. C.* **94**, 2078–2084 (2010).
68. Kang, L. et al. Thermochromic properties and low emissivity of ZnO:Al/VO_2 double-layered films with a lowered phase transition temperature. *Sol. Energ. Mat. Sol. C.* **95**, 3189–3194 (2011).
69. Zhang, Z. et al. Thermochromic VO_2 thin films: solution-based processing, improved optical properties, and lowered phase transformation temperature. *Langmuir* **26**, 10738–10744 (2010).
70. Zhang, Z. et al. Solution-based fabrication of vanadium dioxide on F:SnO_2 substrates with largely enhanced thermochromism and low-emissivity for energy-saving applications. *Energ. Environ. Sci.* **4** https://doi.org/10.1039/c1ee02092g (2011).
71. Wang, S. et al. Thermochromic smart windows with highly regulated radiative cooling and solar transmission. *Nano Energy* **89**, 106440 (2021).
72. Beaini, R. et al. Thermochromic VO_2-based smart radiator devices with ultralow refractive index cavities for increased performance. *Sol. Energ. Mat. Sol. C.* **205**, 110260 (2020).
73. Haddad, E. et al. *In 43rd International Conference on Environmental Systems International Conference on Environmental Systems (ICES)* (American Institute of Aeronautics and Astronautics, 2013).
74. Ito, K. et al. Inverting the thermal radiative contrast of vanadium dioxide by metasurfaces based on localized gap-plasmons. *APL Photonics* **3**, 086101 (2018).
75. Morsy, A. M. et al. Experimental demonstration of dynamic thermal regulation using vanadium dioxide thin films. *Sci. Rep.* **10**, 13964 (2020).
76. Ono, M. et al. Self-adaptive radiative cooling based on phase change materials. *Opt. Express* **26**, A777–A787 (2018).
77. Sun, K. et al. VO_2 Thermochromic metamaterial-based smart optical solar reflector. *ACS Photonics* **5**, 2280–2286 (2018).
78. Wang, X. et al. Fabrication of VO_2-based multilayer structure with variable emittance. *Appl. Surf. Sci.* **344**, 230–235 (2015).

Acknowledgements

Financial supports of this research from the National Key Research and Development Program of China (2022YFA1205200) and the National Natural Science Foundation of China (52033003) are appreciated.

Author contributions

H. Tu and L. Wu conceived the idea and designed the models and experiments. H. Tu performed the material preparation and characterization, H. Tu and T. Wang performed the modeling work. H. Tu wrote the paper. L. Wu and T. Wang revised the article. All the authors (H. Tu, L. Wu, T. Wang, and M. Chen) provided discussion and comments.

Competing interests

The authors declare no competing interests.

Additional information

Supplementary information The online version contains supplementary material available at https://doi.org/10.1038/s41467-025-62432-3.

Correspondence and requests for materials should be addressed to Tong Wang or Limin Wu.

Peer review information *Nature Communications* Yi Long, Qiaoqiang Gan, and the other anonymous reviewer(s) for their contribution to the peer review of this work. A peer review file is available.